

Euclid preparation. XXXIV. The effect of linear redshift-space distortions in photometric galaxy clustering and its cross-correlation with cosmic shear

Euclid Collaboration: K. Tanidis^{1,2*}, V. F. Cardone^{3,4}, M. Martinelli^{3,4}, I. Tutusaus^{5,6}, S. Camera^{7,8,9}, N. Aghanim¹⁰, A. Amara¹¹, S. Andreon¹², N. Auricchio¹³, M. Baldi^{14,13,15}, S. Bardelli¹³, E. Branchini^{16,17}, M. Brescia^{18,19}, J. Brinchmann²⁰, V. Capobianco⁹, C. Carbone²¹, J. Carretero^{22,23}, S. Casas²⁴, M. Castellano³, S. Cavuoti^{19,25}, A. Cimatti²⁶, R. Cledassou^{27,28**}, G. Congedo²⁹, L. Conversi^{30,31}, Y. Copin³², L. Corcione⁹, F. Courbin³³, H. M. Courtois³⁴, A. Da Silva^{35,36}, H. Degaudenzi³⁷, J. Dinis^{36,35}, F. Dubath³⁷, X. Dupac³¹, S. Dusini³⁸, M. Farina³⁹, S. Farrens⁴⁰, S. Ferriol³², P. Fosalba^{41,42}, M. Frailis⁴³, E. Franceschi¹³, M. Fumana²¹, S. Galeotta⁴³, B. Garilli²¹, W. Gillard⁴⁴, B. Gillis²⁹, C. Giocoli^{13,15}, A. Grazian⁴⁵, F. Grupp^{46,47}, L. Guzzo^{48,12,49}, S. V. H. Haugan⁵⁰, W. Holmes⁵¹, I. Hook⁵², A. Hornstrup^{53,54}, K. Jahnke⁵⁵, B. Joachimi⁵⁶, E. Keihänen⁵⁷, S. Kermiche⁴⁴, A. Kiessling⁵¹, M. Kunz⁶, H. Kurki-Suonio^{58,59}, P. B. Lilje⁵⁰, V. Lindholm^{58,59}, I. Lloro⁶⁰, E. Maiorano¹³, O. Mansutti⁴³, O. Marggraf⁶¹, K. Markovic⁵¹, N. Martinet⁶², F. Marulli^{63,13,15}, R. Massey⁶⁴, S. Maurogordato⁶⁵, E. Medinaceli¹³, S. Mei⁶⁶, M. Meneghetti^{13,15}, G. Meylan³³, M. Moresco^{63,13}, L. Moscardini^{63,13,15}, E. Munari⁴³, S.-M. Niemi⁶⁷, C. Padilla²², S. Paltani³⁷, F. Pasian⁴³, K. Pedersen⁶⁸, W. J. Percival^{69,70,71}, V. Pettorino⁷², S. Pires⁴⁰, G. Polenta⁷³, J. E. Pollack^{74,66}, M. Poncet²⁷, L. A. Popa⁷⁵, F. Raison⁴⁶, A. Renzi^{76,38}, J. Rhodes⁵¹, G. Riccio¹⁹, E. Romelli⁴³, M. Roncarelli¹³, E. Rossetti¹⁴, R. Saglia^{77,46}, D. Sapone⁷⁸, B. Sartoris^{77,43}, M. Schirmer⁵⁵, P. Schneider⁶¹, A. Secroun⁴⁴, G. Seidel⁵⁵, S. Serrano^{42,41,79}, C. Sirignano^{76,38}, G. Sirri¹⁵, L. Stanco³⁸, P. Tallada-Crespi^{80,23}, A. N. Taylor²⁹, I. Tereno^{35,81}, R. Toledo-Moreo⁸², F. Torradeflot^{23,80}, E. A. Valentijn⁸³, L. Valenziano^{13,84}, T. Vassallo^{77,43}, A. Veropalumbo¹², Y. Wang⁸⁵, J. Weller^{77,46}, G. Zamorani¹³, J. Zoubian⁴⁴, E. Zucca¹³, A. Biviano^{43,86}, A. Boucaud⁶⁶, E. Bozzo³⁷, C. Colodro-Conde⁸⁷, D. Di Ferdinando¹⁵, R. Farinelli¹³, J. Graciá-Carpio⁴⁶, S. Marcin⁸⁸, N. Mauri^{26,15}, V. Scottez^{89,90}, M. Tenti⁸⁴, A. Tramacere³⁷, Y. Akrami^{91,92,93,94,95}, V. Allevato^{19,96}, C. Baccigalupi^{97,43,98}, A. Balaguera-Antolínez^{87,99}, M. Ballardini^{100,101,13}, D. Benielli⁴⁴, F. Bernardeau^{102,103}, S. Borgani^{43,104,98,86}, A. S. Borlaff^{105,106}, C. Burigana^{107,84}, R. Cabanac⁵, A. Cappi^{13,65}, C. S. Carvalho⁸¹, G. Castignani^{63,13}, T. Castro^{43,98,86}, G. Cañas-Herrera^{67,108}, K. C. Chambers¹⁰⁹, A. R. Cooray¹¹⁰, J. Coupon³⁷, A. Díaz-Sánchez¹¹¹, S. Davini¹⁷, S. de la Torre⁶², G. De Lucia⁴³, G. Desprez¹¹², S. Di Domizio¹¹³, H. Dole¹⁰, J. A. Escartin Vigo⁴⁶, S. Escoffier⁴⁴, P. G. Ferreira², I. Ferrero⁵⁰, F. Finelli^{13,84}, L. Gabarra^{76,38}, J. García-Bellido⁹¹, E. Gaztanaga^{41,42,11}, F. Giacomini¹⁵, G. Gozaliasl^{58,114}, H. Hildebrandt¹¹⁵, S. Ilić^{116,27,5}, J. J. E. Kajava^{117,118}, V. Kansal¹¹⁹, C. C. Kirkpatrick⁵⁷, L. Legrand⁶, A. Loureiro^{120,95}, J. Macias-Perez¹²¹, M. Magliocchetti³⁹, G. Mainetti¹²², R. Maoli^{123,3}, C. J. A. P. Martins^{124,20}, S. Matthew²⁹, L. Maurin¹⁰, R. B. Metcalf⁶³, M. Migliaccio^{125,126}, P. Monaco^{104,43,98,86}, G. Morgante¹³, S. Nadathur¹¹, A. A. Nucita^{127,128,129}, M. Pöntinen⁵⁸, L. Patrizii¹⁵, A. Pezzotta⁴⁶, V. Popa⁷⁵, D. Potter¹³⁰, A. G. Sánchez⁴⁶, Z. Sakr^{131,5,132}, J. A. Schewtschenko²⁹, A. Schneider¹³⁰, M. Sereno^{13,15}, P. Simon⁶¹, A. Spurio Mancini¹³³, J. Steinwagner⁴⁶, M. Tewes⁶¹, R. Teyssier¹³⁴, S. Toft^{54,135,136}, J. Valiviita^{58,59}, M. Viel^{86,43,97,98}, L. Linke¹³⁷

(Affiliations can be found after the references)

April 23, 2024

ABSTRACT

Context. The cosmological surveys that are planned for the current decade will provide us with unparalleled observations of the distribution of galaxies on cosmic scales, by means of which we can probe the underlying large-scale structure (LSS) of the Universe. This will allow us to test the concordance cosmological model and its extensions. However, precision pushes us to high levels of accuracy in the theoretical modelling of the LSS observables, so that no biases are introduced into the estimation of the cosmological parameters. In particular, effects such as redshift-space distortions (RSD) can become relevant in the computation of harmonic-space power spectra even for the clustering of the photometrically selected galaxies, as has previously been shown in literature.

Aims. In this work, we investigate the contribution of linear RSD, as formulated in the Limber approximation by a previous work, in forecast cosmological analyses with the photometric galaxy sample of the *Euclid* survey. We aim to assess their impact and to quantify the bias on the measurement of cosmological parameters that would be caused if this effect were neglected.

Methods. We performed this task by producing mock power spectra for photometric galaxy clustering and weak lensing, as is expected to be obtained from the *Euclid* survey. We then used a Markov chain Monte Carlo approach to obtain the posterior distributions of cosmological parameters from these simulated observations.

Results. When the linear RSD is neglected, significant biases are caused when galaxy correlations are used alone and when they are combined with cosmic shear in the so-called 3×2pt approach. These biases can be equivalent to as much as 5σ when an underlying Λ CDM cosmology is assumed. When the cosmological model is extended to include the equation-of-state parameters of dark energy, the extension parameters can be shifted by more than 1σ .

Key words. Cosmology: theory – large-scale structure of the Universe – cosmological parameters

1. Introduction

Within the current decade, several large-scale structure (LSS) surveys are expected to start their operations or to release their first results. They will provide a significant improvement to available cosmological data sets. These forthcoming LSS surveys will map the matter distribution in the Universe with exquisite precision. Some of the surveys will be ground-based, such as the Dark Energy Spectroscopic Instrument (DESI, DESI Collaboration: Aghamousa et al. 2016a,b), the Legacy Survey of Space and Time (LSST) at the Vera C. Rubin Observatory (LSST Science Collaboration: Abell et al. 2009; LSST Dark Energy Science Collaboration: Mandelbaum et al. 2018; Ivezić et al. 2019), and the Square Kilometre Array Observatory (SKAO; see, e.g., Abdalla et al. 2015; Santos et al. 2015; Brown et al. 2015; Bull et al. 2015; Camera et al. 2015b; Raccanelli et al. 2015; SKA Cosmology Science Working Group 2020). Others will be space-borne, such as the *Euclid* satellite (Laureijs et al. 2011; Amendola et al. 2013, 2018; Euclid Collaboration: Blanchard et al. 2020), the *Nancy Grace Roman* Space Telescope (Spergel et al. 2015), and the Spectro-Photometer for the History of the Universe, Epoch of Reionization, and Ices Explorer (SPHEREx; see, e.g., Doré et al. 2014, 2018).

All these surveys rely on the observation of galaxy positions and shapes, with which summary statistics can be constructed that are customarily referred to in cosmology as galaxy clustering (GC) and weak lensing (WL). This can be done in multiple ways, using either the real-space 2pt correlation function, or the harmonic-space power spectrum that we study here, or even via other statistics such as COSEBIs (Schneider et al. 2010), or higher-order statistics (Euclid Collaboration: Ajani et al. 2023). The GC encodes information on the clustering of matter due to the effect of gravity, while the WL provides information on the projected matter distribution through its gravitational lensing effect.

In this work, we focus on *Euclid* and its surveys.¹ *Euclid* is a European Space Agency medium-class space mission whose launch took place on 1 July 2023. It will perform photometric and spectroscopic galaxy surveys over an area of $\sim 15000 \text{ deg}^2$ of the extragalactic sky (Laureijs et al. 2011), with the near-infrared instrument (Costille et al. 2018) and the visible imager (Cropper et al. 2018), which will be carried on board. The photometric survey will measure the positions and shapes of over a billion galaxies, enabling the analysis of photometric GC (GCph) and WL. Because the photometric measurements will provide relatively uncertain redshift measurements (compared to spectroscopic observations), the analyses of these observables will be performed via a tomographic approach by binning galaxies in redshift slices and considering the projected two-dimensional data sets. The precise radial measurements of the spectroscopic survey will instead allow us to perform a spectroscopic GC (GCsp) analysis, that is, a galaxy-clustering analysis in three dimensions.

In Euclid Collaboration: Blanchard et al. (2020, ‘Euclid preparation: VII’, hereafter EP:VII), the constraints expected from *Euclid* have been forecast for the individual GCsp, GCph, and WL probes and also for their combination. To obtain these results, EP:VII used several assumptions to simplify the theoretical computation of observables: the Limber approximation was used for all the photometric observables, and it was assumed for GCph that the only non-negligible contribution to the galaxy position correlation function comes from the anisotropies in the density field. It is known, however, that several other effects contribute to GCph, including lensing magnification, velocity, and relativistic effects (Yoo 2010; Challinor & Lewis 2011; Bonvin & Durrer 2011).

These various contributions can be significant at very large scales, which we define as scales corresponding to a wavenumber smaller than that at which the matter power spectrum peaks at the matter-radiation equality scale. These scales are effectively within reach of wide surveys such as *Euclid*, and it has been shown that neglecting them could lead to inaccurate results. The cosmology that is recovered through parameter estimation pipelines might be significantly biased with respect to the true underlying cosmology (Camera et al. 2015a; Tanidis & Camera 2019; Tanidis et al. 2019; Martinelli et al. 2022; Lepori et al. 2022).

In this work, we focus on one of the most important effects, namely redshift-space distortion (RSD). We also aim specifically to quantify its impact on the expected results of the *Euclid* wide survey. The effect of the linear RSD on the angular clustering is not new and has been thoroughly studied before (Scharf et al. 1994; Heavens & Taylor 1995; Padmanabhan et al. 2007; Blake et al. 2007; Nock et al. 2010; Crocce et al. 2011; Balaguera-Antolínez et al. 2018; Tanidis & Camera 2019). The effects have also been included in the Dark Energy Survey (DES, DES Collaboration: Abbott et al. 2005) 3×2pt data analysis for Y3 in the configuration space (Abbott et al. 2022), although they were initially neglected in the Y1 analysis for the GC in the configuration and harmonic space (Elvin-Poole et al. 2018; Andrade-Oliveira et al. 2021). Here, we apply the approach of Tanidis & Camera (2019), where the linear RSD contribution to GC harmonic-space power spectra is obtained within the Limber approximation. We examine this contribution to the *Euclid* wide survey. This allows us to compute the theoretical prediction at a reasonable speed so that it can be used to estimate the parameters. Moreover, we only focus on GCph and do not discuss GCsp at all. We therefore always refer to the GCph probe simply as GC throughout.

The paper is organised as follows. The equations we used to compute the theoretical predictions for the observables of interest are reviewed in Sect. 2, where we also outline how RSD enters the calculations. In Sect. 2.4 we summarise the results of the Flagship simulation galaxy catalogue. Our analysis method is shown in Sect. 3 and the results we obtained are provided in Sect. 4. We finally summarise our conclusions in Sect. 5.

* e-mail: konstantinos.tanidis@physics.ox.ac.uk

** Deceased

¹ <http://www.euclid-ec.org/>.

2. Photometric observables in *Euclid*

2.1. Harmonic-space power spectra

The harmonic-space power spectrum $C_\ell^{AB}(z_i, z_j)$ between an observable A in the redshift bin i and an observable B in the redshift bin j is defined as

$$\langle A_{i,\ell m} B_{j,\ell' m'}^* \rangle = C_\ell^{AB}(z_i, z_j) \delta_{\ell\ell'}^K \delta_{mm'}^K, \quad (1)$$

where $X_{\ell m}$ are the coefficients of the harmonic expansion of observable X , and δ^K denotes the Kronecker symbol. Here, the letters A and B stand for the observables of interest: galaxy number count fluctuations, Δ , or galaxy ellipticities, ϵ . Both fields are discussed in more detail in Sect. 2.2 and Sect. 2.3, respectively.

Within the Limber approximation (Kaiser 1992), which is valid at $\ell \gg 1$ and for broad redshift kernels, the harmonic-space (also called angular) power spectrum between two observables A and B is

$$C_{ij}^{AB}(\ell) = \int \frac{dr}{r^2} W_i^A(\ell, r) W_j^B(\ell, r) P_{\delta\delta} \left(k = \frac{\ell + 1/2}{r}, r \right), \quad (2)$$

where $P_{\delta\delta}$ is the (non-linear) matter power spectrum, $k = |\mathbf{k}|$ is the wave number, which is the Fourier mode related to the comoving separation between pairs of galaxies in configuration space, and $r(z)$ is the radial comoving distance to redshift z for a flat cosmology. The generic redshift-binned kernel $W_i^A(\ell, r)$ takes different forms depending on the target observables, as we show in Sect. 2.2 and Sect. 2.3. We use the notation $C_{ij}^{AB}(\ell)$ as in EP:VII, as opposed to $C_\ell^{AB}(z_i, z_j)$ of Eq. (1), to denote the fact that we refer to the Limber-approximated power spectrum.

2.2. Linear RSD in GCph

In GC, galaxies are biased tracers of the underlying matter field (Kaiser 1987). At sufficiently large scales, the bias can be considered to only depend on redshift and not on scale (Abbott et al. 2018). On the other hand, when non-linear scales are added, the galaxy bias becomes non-local and a specific treatment is required to account for this effect (Sánchez et al. 2016; Desjacques et al. 2018). In addition, RSDs are additional observational effects due to the peculiar velocities of galaxies (Kaiser 1987; Szalay et al. 1998). These are customarily split into linear RSD (also known as the Kaiser effect) and non-linear RSD (also known as the fingers of God, ‘FoG’ hereafter). The former causes the squashing of the galaxy 2pt correlation function on large scales in the direction perpendicular to the line of sight, while the latter enhances the clustering amplitude along the line-of-sight direction on small scales. In the current analysis we consider a simple model, that assumes that the galaxy bias is linear and scale independent, and we only account for linear RSD. The modelling of the non-linear galaxy bias and the FoG as well as their effects in the photometric observables for *Euclid* is left for future work. The kernel of Eq. (2) for the GC that includes up to linear RSD in the Limber approximation (for details, see Tanidis & Camera 2019) takes the form

$$W_i^A(\ell, r) = W_i^{\text{den}}(r) + W_i^{\text{RSD}}(\ell, r), \quad (3)$$

with the first term being due to fluctuations in the density field,

$$W_i^{\text{den}}(r) = n_i(r) b_i(r), \quad (4)$$

with $n_i(r) dr$ the galaxy probability density in bin i between the comoving distance r and $r + dr$, and b_i being the corresponding linear galaxy bias, computed at $r \equiv r(z)$. We treat this as a

constant within the redshift bin, and its actual amplitude is a nuisance parameter, over which we marginalised in our analysis. For the fiducial galaxy bias values in each bin (see Table 2), we used the fiducial model of *Euclid* Collaboration: Pocino et al. (2021), ‘*Euclid* Collaboration: XII’, hereafter EP:XII, who considered a magnitude cut at $I_e = 24.5$ for the *Euclid* imager, which will observe through an optical broad band. For the galaxy distributions $n_i(r)$, we used the outcome of the Flagship galaxy simulation of the *Euclid* Consortium, for which we provide details in Sect. 2.4.

The second term in Eq. (3) is the RSD contribution (Tanidis & Camera 2019),

$$W_i^{\text{RSD}}(\ell, r) = \sum_{n=-1}^1 L_n(\ell) n_i \left(\frac{2\ell + 1 + 4n}{2\ell + 1} r \right) f \left(\frac{2\ell + 1 + 4n}{2\ell + 1} r \right), \quad (5)$$

with

$$L_0(\ell) = \frac{2\ell^2 + 2\ell - 1}{(2\ell - 1)(2\ell + 3)}, \quad (6)$$

$$L_{-1}(\ell) = -\frac{\ell(\ell - 1)}{(2\ell - 1)\sqrt{(2\ell - 3)(2\ell + 1)}}, \quad (7)$$

$$L_{+1}(\ell) = -\frac{(\ell + 1)(\ell + 2)}{(2\ell + 3)\sqrt{(2\ell + 1)(2\ell + 5)}}. \quad (8)$$

In Eq. (5), $f := -(1+z)d \ln D/dz$ is the growth rate, with D being the linear growth factor. In the top panel of Fig. 1, we quantify the signal loss when the linear RSD are not included in the photometric GC harmonic-space power spectrum. In particular, RSD are important at large scales, for approximately $\ell \lesssim 100$. Additionally, the contribution to the total signal increases with redshift for a given redshift bin width. For example, RSD contribute to the total signal from 2–3% at low redshift (solid purple curve, bin pair 1–1) and gradually increase with increasing redshift (dash-dotted yellow curve, bin pair 6–6) up to ~40% at the lowest available multipoles. However, we should note that this is not true for the highest redshift bin (dotted blue curve, bin pair 13–13). This bin contributes less to the full signal than the bin pairs 10–10 and 6–6, for example, Tanidis et al. (2019) showed that the linear RSD effect is gradually diluted when the width of the redshift bin increases. This is particularly the case for the highest-redshift bins due to the large photometric uncertainties at high redshifts.

Another important correction to the galaxy density field is the magnification bias. We wish to quantify the impact of linear RSD alone on *Euclid* photometric observables here and therefore neglected the magnification effect in our analysis. However, this effect has been thoroughly studied in Lepori et al. (2022) (in that study the linear RSD were neglected), and its inclusion was found to be crucial to avoid biases on the cosmological parameter estimation for *Euclid*. Similar studies of this effect have also been conducted for other future experiments (Tanidis et al. 2019).

In addition, there are also local and integrated contributions to the signal that are measurable at ultra-large scales, such as the Doppler terms, the Sachs-Wolfe and the integrated Sachs-Wolfe effects, and the time delay. We neglected these contributions in our analysis because for $\ell \gg 1$, where the Limber approximation holds, their effect is negligible (Yoo 2010; Challinor & Lewis 2011; Bonvin & Durrer 2011; Martinelli et al. 2022).

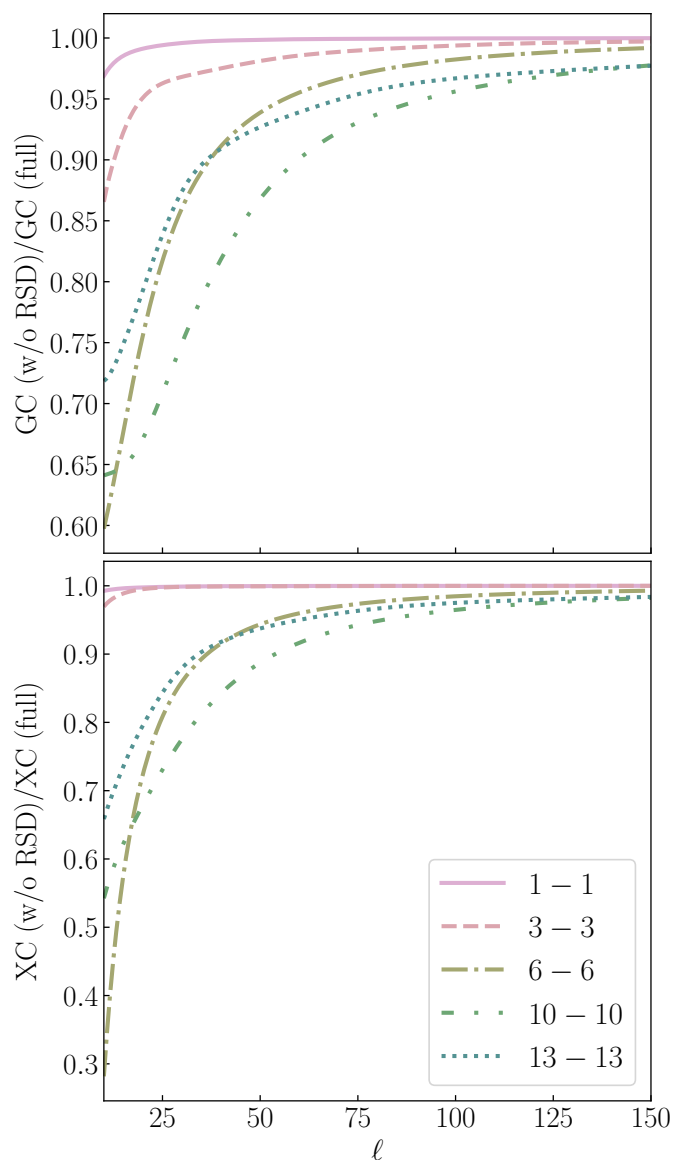


Fig. 1. Ratio of the harmonic-space power spectrum for the density fluctuations alone with respect to that including RSD for some tomographic auto-bin correlations ($i = j$). *Top:* GC. *Bottom:* XC.

2.3. Cosmic shear

The LSS of the Universe deflects the paths of photons that are emitted by distant sources. This distorts the source images. This distortion is decomposed into the convergence, κ , and shear, γ , which correspond to size magnification and shape distortion of the images, respectively, and are related linearly. Both signals contain useful cosmological information, but the former is more impossible to extract because it requires knowledge of the original source sizes (Heavens et al. 2013; Alsing et al. 2015). For this reason, shear is the usual focus of WL surveys of the LSS.

The harmonic-space power spectrum of the shear field is a probe of the growth of structures and the cosmological expansion. In addition to the cosmic shear, the correlation of the galaxy shapes also receives a contribution from intrinsic alignments (hereafter IA), which in the context of cosmological WL studies is regarded as a systematic effect. This accounts for the fact that, in addition to the random orientations of galaxies, which ideally would make the ellipticity an unbiased estimator of the

shear field, there are also IA of the galaxies that are caused by the tidal interactions during galaxy formation, and also astrophysical effects that contaminate the WL analysis (Joachim et al. 2015).

For the WL sample, the kernel of the observed ellipticity power spectrum including cosmic shear γ and IA, reads

$$W_i^\varepsilon(\ell, r) = W_i^\gamma(\ell, r) + W_i^{\text{IA}}(r). \quad (9)$$

The shear contribution is

$$W_i^\gamma(\ell, r) = \frac{3 L_\gamma(\ell) \Omega_{\text{m},0} H_0^2}{2c^2} [1 + z(r)] r q_i(r), \quad (10)$$

where c is the vacuum speed of light, $q_i(r)$ is the so-called lensing efficiency for a flat Universe,

$$q_i(r) = \int_r^\infty dr' \frac{r' - r}{r'} n_i(r'), \quad (11)$$

and the ℓ -dependent factor is given by

$$L_\gamma(\ell) = \sqrt{\frac{(\ell + 2)!}{(\ell - 2)!}} \left(\frac{2}{2\ell + 1} \right)^2. \quad (12)$$

For WL we also used the $n_i(r)$ obtained from the Flagship simulation of Sect. 2.4. Because we restricted our analysis to multipoles, for which the Limber approximation applies ($\ell \gg 1$), this factor can be considered to be $L_\gamma(\ell) \approx 1$.

The IA contribution can instead be modelled as in EP:VII, namely

$$W_i^{\text{IA}}(r) = -\mathcal{A}_{\text{IA}} C_{\text{IA}} \Omega_{\text{m},0} \frac{\mathcal{F}_{\text{IA}}[z(r)]}{D[z(r)]} n_i(r), \quad (13)$$

where

$$\mathcal{F}_{\text{IA}}(z) = (1 + z)^{\eta_{\text{IA}}} \left[\frac{\langle L \rangle(z)}{L_*(z)} \right]^{\beta_{\text{IA}}}. \quad (14)$$

The amplitude and shape of the IA signal is captured by the nuisance parameters \mathcal{A}_{IA} , β_{IA} and η_{IA} (see Table 2 for their fiducial values), with C_{IA} kept fixed at the value 0.0134 because it is degenerate with \mathcal{A}_{IA} . The terms $\langle L \rangle(z)$ and $L_*(z)$ denote the mean and the characteristic luminosity of the source galaxies with respect to redshift.² We neglected other sources of systematic effects for the WL probe such as the shear bias and the photometric redshift uncertainties (which are also present for the tomographic bins in photometric GC in principle).

In the bottom panel of Fig. 1 we show the signal loss when we neglect the linear RSD contribution in the cross power spectrum between GC and WL (hereafter XC). The picture is very similar compared to the one presented for the GC (top panel of Fig. 1). The main difference is that the RSD contribution to the total signal is lower than $\sim 1\%$ at the lowest redshift (bin pair 1–1), reaching a maximum of up to $\sim 70\%$ in bin pair 6–6 at the largest scales.

For some bin cases, the signal that is lost when the RSD is neglected with respect to the total signal in XC is more than the GC, which indeed seems to be counter-intuitive because the RSD is an additional term in the GC kernel Eq. (3). Although it is true that the RSD kernel given by Eq. (5) appears twice in Eq. (2) for all bin correlations due to Eq. (3) and only once in the XC, the GC spectra have more power than the XC spectra, as shown in Fig. 2. The WL kernel of Eq. (9) also appears once in the XC, and this kernel lowers the signal. For this reason, the XC spectra might be numerically more strongly affected when the RSD signal stronger, as in the bin correlations 6–6 and 10–10.

² We refer the reader to EP:VII for more details concerning the IA modelling.

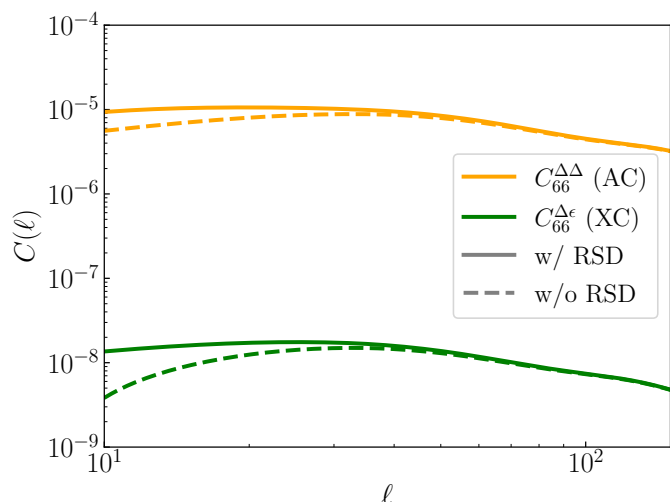


Fig. 2. GC (orange) and the XC (green) spectrum for the bin correlation 6–6. The dashed lines correspond to spectra without RSD, and the solid lines show spectra with RSD.

2.4. The *Euclid* Flagship simulation

In order to create realistic mock data vectors for our analysis, we used the simulated results from the Flagship galaxy simulation of the *Euclid* Consortium (*Euclid* Consortium, in preparation). The galaxy catalogue was produced using the N -body Flagship dark matter simulation (Potter et al. 2017) with a Λ CDM fiducial cosmology given by the total matter abundance, $\Omega_{m,0} = 0.319$; the baryon abundance, $\Omega_{b,0} = 0.049$; the r.m.s. variance of the linear matter fluctuations at $z = 0$ in spheres with a radius of $8 h^{-1}$ Mpc, $\sigma_8 = 0.830$; the spectral index of the primordial curvature power spectrum, $n_s = 0.96$; and the dimensionless Hubble constant, $h \equiv H_0/(100 \text{ km s}^{-1} \text{ Mpc}^{-1}) = 0.67$. The N -body simulation ran a box of $3.78 h^{-1}$ Gpc with a particle mass of $2.398 \times 10^9 h^{-1} M_\odot$.

The dark matter haloes were identified using ROCKSTAR (Behroozi et al. 2013) down to masses of $2.4 \times 10^{10} h^{-1} M_\odot$ (corresponding to ten particles per halo). Then, the galaxies were assigned to the haloes using the halo-occupation distribution and the halo-abundance matching methods, following the recipe presented in Carretero et al. (2015). Several observational constraints were used to calibrate the galaxy mocks including the luminosity function (Blanton et al. 2003; Blanton et al. 2005) applied for the faint galaxies, the measurements of galaxy clustering as a function of colour and luminosity (Zehavi et al. 2011), and the colour-magnitude diagram from Blanton et al. (2005). The final galaxy catalogue contains almost 3.4 billion galaxies over 5000 deg^2 and extends up to redshift 2.3.

We followed the analysis of EP:XII, where an optimisation of the galaxy sample for photometric GC analyses was performed using the Flagship simulation. EP:XII generated photometric redshift estimates with the directional-neighbourhood-fitting training-based algorithm (De Vicente et al. 2016) for all galaxies within a patch of 400 deg^2 of the Flagship simulation up to a magnitude limit of 25 in the VIS band. We considered the fiducial sample from EP:XII. This corresponds to a training of the algorithm with an incomplete spectroscopic training sample to mimic the lack of spectroscopic information at very faint magnitudes, and to optimistic magnitude limits for all photometric bands. There is an additional selection of objects with magnitudes brighter than 24.5 in the VIS band. By using the directional-neighbourhood-fitting algorithm, two different esti-

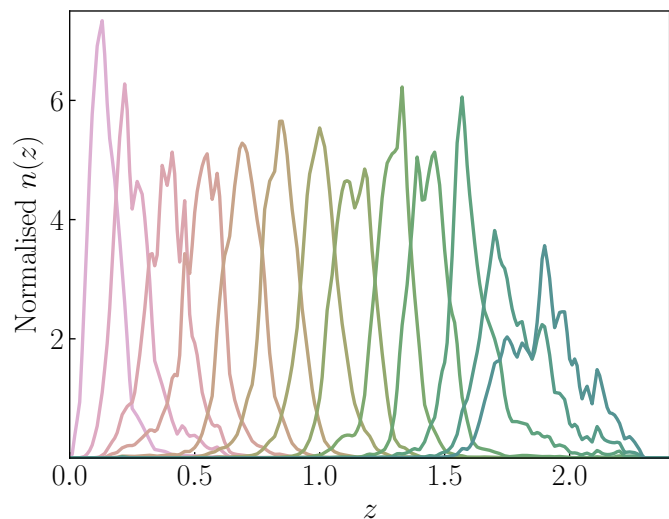


Fig. 3. Normalised number densities of the 13 tomographic equispaced bins with redshift from the *Euclid* Flagship simulation (EP:XII).

Table 1. Fiducial values of the cosmological parameters.

$\Omega_{m,0}$	$\Omega_{b,0}$	h	σ_8	n_s	w_0	w_a
0.320	0.050	0.67	0.816	0.96	-1.0	0.0

mates for the photometric redshift are provided for each object. One estimate is the average of the redshifts from the neighbourhood, which we denote z_{mean} . The second estimate is a Monte Carlo draw from the nearest neighbour, and we denote this z_{mc} . We refer to EP:XII and De Vicente et al. (2016) for the similarities and differences between these two estimates. The final sample was then composed of 13 tomographic equispaced bins in z_{mean} up to $z = 2$, that is, 13 bins with a constant redshift width in z_{mean} , and therefore, with a different width in z_{mc} . The normalised number densities of these bins as a function of redshift are shown in Fig. 3. In addition to the galaxy distributions, we also considered the linear galaxy biases for each of these distributions, which are provided in EP:XII.

3. Synthetic data and analysis method

In order to quantify the impact of linear RSD on the photometric observables of *Euclid*, we created mock data that we compared with our theoretical predictions. For this purpose, we computed the power spectra for GC, WL, and XC following Eq. (2) in a fiducial cosmology. We chose this to be the same as EP:VII, namely a flat Λ CDM model with one massive and two massless neutrinos fixed to $\sum m_\nu = 0.06 \text{ eV}$. The fiducial values for the parameters are shown in Table 1 and Table 2.

We modelled the matter power spectrum, $P_{\delta\delta}$, on non-linear small scales using *halofit* (Smith et al. 2003), including corrections for both dark energy (Takahashi et al. 2012) and massive neutrinos (Bird et al. 2012) as in EP:VII. Using these assumptions, we can compute the harmonic-space power spectra of Eq. (2) for photometric GC, WL, and XC. These represent our synthetic data set, against which we can compare theoretical predictions from different models to constrain model parameters. In order to do this, we obtained the χ^2 for any set of parameters θ including cosmological and nuisance, and assumed the Gaussian likelihood

$$\chi^2(\theta) = [d - t(\theta)]^T C^{-1} [d - t(\theta)] . \quad (15)$$

Table 2. Fiducial values of the nuisance parameters.

b_1	b_2	b_3	b_4	b_5	b_6	b_7	b_8	b_9	b_{10}	b_{11}	b_{12}	b_{13}	\mathcal{A}_{IA}	β_{IA}	η_{IA}
1.025	1.037	1.066	1.110	1.198	1.293	1.429	1.559	1.758	1.947	2.217	2.537	2.738	1.72	2.17	-0.41

Note: The linear galaxy bias parameter per redshift bin i for GC is denoted with b_i and the WL parameters for the whole redshift range with \mathcal{A}_{IA} , β_{IA} , and η_{IA} (for the resources of the IA modelling, see again EP:VII.). The centres of the redshift bins are the following: $\bar{z}_1 = 0.14$, $\bar{z}_2 = 0.26$, $\bar{z}_3 = 0.39$, $\bar{z}_4 = 0.53$, $\bar{z}_5 = 0.69$, $\bar{z}_6 = 0.84$, $\bar{z}_7 = 1.0$, $\bar{z}_8 = 1.14$, $\bar{z}_9 = 1.3$, $\bar{z}_{10} = 1.44$, $\bar{z}_{11} = 1.62$, $\bar{z}_{12} = 1.78$ and $\bar{z}_{13} = 1.72$.

The data vector \mathbf{d} , the vector of theoretical predictions $\mathbf{t}(\boldsymbol{\theta})$, and the covariance matrix \mathbf{C} (which is assumed to be constant and independent of the cosmological parameters), were all stacked along the i , j , and ℓ indices.

The covariance matrix of the data, \mathbf{C} , is the flattened version of the fourth-order Gaussian covariance (as in EP:VII), namely,

$$\text{Cov} \left[C_{ij}^{AB}(\ell), C_{mm}^{A'B'}(\ell') \right] = \frac{\widetilde{C}_{im}^{AA'}(\ell) \widetilde{C}_{jn}^{BB'}(\ell) + \widetilde{C}_{in}^{AB'}(\ell) \widetilde{C}_{jm}^{BA'}(\ell)}{(2\ell + 1) \Delta\ell f_{\text{sky}}} \delta_{\ell\ell'}^{\text{K}},$$

with $\widetilde{C}_{ij}^{AB}(\ell) = C_{ij}^{AB}(\ell) + N_{ij}^{AB}(\ell)$, and $N_{ij}^{AB}(\ell)$ being the noise contribution to the measurement, and $f_{\text{sky}} = 0.3636$ is the sky fraction observed by *Euclid*. Finally, we used

$$N_{ij}^{\Delta\Delta}(\ell) = \frac{1}{\bar{n}_i} \delta_{ij}^{\text{K}}, \quad (17)$$

$$N_{ij}^{\epsilon\epsilon}(\ell) = \frac{\sigma_\epsilon^2}{\bar{n}_i} \delta_{ij}^{\text{K}}, \quad (18)$$

$$N_{ij}^{\Delta\epsilon}(\ell) = 0, \quad (19)$$

with \bar{n}_i being the number density of galaxies per steradian in each tomographic bin and σ_ϵ^2 the intrinsic ellipticity variance, which we assumed to be $\sigma_\epsilon = 0.3$ (as in EP:VII).

We binned our data in multipoles considering $N_\ell = 20$ log-spaced multipole bins in the range $\{\ell_{\text{min}}, \ell_{\text{max}}\}$, with $\Delta\ell$ the width of each bin. We considered the lowest multipole to be $\ell_{\text{min}} = 10$ and considered an optimistic and a pessimistic scenario for the maximum multipole cut ℓ_{max} (see EP:VII), with

- Optimistic | pessimistic GC: 3000 | 750,
- Optimistic | pessimistic WL: 5000 | 1500.

For XC, we conservatively considered the smallest ℓ_{max} (corresponding to the GC values).

The assumptions we adopted from EP:VII for the purposes of this work in our modelling are not expected to affect the results strongly. For example, an increase in σ_ϵ would have an effect on the WL part but not on the GC and XC. Then, a decrease in \bar{n}_i would increase the shot noise, but the GC part of the analysis, which is what we are most interested in, with the linear RSD scales, should not be dominated by shot noise. Therefore, the $3 \times 2\text{pt}$ contours would increase through the WL contribution, but would not change our conclusions on RSD.

With this approach, we needed only one additional ingredient to obtain the χ^2 of Eq. (15), which is the theory vector $\mathbf{t}(\boldsymbol{\theta})$. We chose to focus on two models to be constrained with our mock data, which we refer to as ΛCDM and $w_0w_a\text{CDM}$ flat cosmologies following the same modelling as in EP:VII. The former has five free cosmological parameters, which are $\Omega_{\text{m},0}$, $\Omega_{\text{b},0}$, h , σ_8 , and n_s . The latter also includes the equation-of-state parameters of dark energy, w_0 and w_a , which come from the CPL parametrisation (Chevallier & Polarski 2001; Linder 2003),

$$w(z) = w_0 + w_a \frac{z}{1+z}. \quad (20)$$

Article number, page 6 of 15

As nuisance parameters, both models feature for the GC, the linear galaxy bias amplitudes b_i (see Sect. 2.2), and for the WL, the IA modelling parameters \mathcal{A}_{IA} , β_{IA} , and η_{IA} (see Sect. 2.3).

4. Results

In this section, we use the method presented in Sect. 3 to investigate the impact of the RSD contribution, modelled as in Sect. 2.2, on the final cosmological constraints. We explore the (16) parameter space with a Markov chain Monte Carlo (MCMC) approach using *emcee* (Foreman-Mackey et al. 2013), and we obtain from *CAMB* (Lewis et al. 2000; Howlett et al. 2012) all the quantities needed to compute the theoretical predictions following Eq. (2) in a modified version of the code *CosmoSIS* (Zuntz et al. 2015). We adopt improper (flat) priors for all the parameters in Table 1 and Table 2.

4.1. Validation

Before we proceeded to set up the realistic and computationally expensive MCMC chains for all the different cosmologies and scenarios, we first ran a single case with an MCMC and compared it to a Fisher matrix forecast (see EP:VII, for details about Fisher forecasts and their derivatives accuracy) in order to validate the pipeline. In brief, entries of the Fisher matrix are constructed as

$$F_{\alpha\beta} = \frac{\partial \mathbf{t}^T}{\partial \theta_\alpha} \mathbf{C}^{-1} \frac{\partial \mathbf{t}}{\partial \theta_\beta}, \quad (21)$$

where $\{\theta_\alpha\}$ are the elements of the parameter vector $\boldsymbol{\theta}$ (see Sect. 3).

In general, the Fisher forecasts, whose computation is usually faster than any Bayesian sampler, are used in order to investigate the likelihood curvature of the parameter hyperspace near its peak. When the posterior is very well described by a Gaussian, the Fisher forecasts are particularly accurate, and the smaller the uncertainties, the closer the peak of the posterior where the Gaussian approximation holds. This applies to forthcoming LSS experiments such as *Euclid*, which will provide us with an unprecedentedly large number of sources that will minimise the resulting errors. As expected, the precision will increase even further when we consider all the available signal. Therefore, we performed a Fisher forecast on the combination of GC, WL, and XC, which we labelled $3 \times 2\text{pt}$. We show this by considering a $w_0w_a\text{CDM}$ cosmological model and an optimistic scale cut, in order to investigate the potential Gaussianity of the posterior in an extended cosmology model with two additional parameters, $\{w_0, w_a\}$. In Eq. (21) we calculated the theory vector \mathbf{t} for the fiducial cosmology model and the covariance matrix \mathbf{C} following Sect. 3. We also included linear RSD as described in Sect. 2.2. With the same assumptions, we repeated the analysis with an MCMC approach, exploring the posterior and then finding the minimum χ^2 over the parameter space $\boldsymbol{\theta}$.

The comparison between the MCMC and Fisher approaches is shown in the top panel of Fig. 4, where the 68% and 95% credibility levels (C.L.) on cosmological parameters are presented, after the bias and IA parameters were marginalised over.³ The filled green contours correspond to the MCMC and the empty orange contours show the Fisher forecast. The agreement between the two is remarkable and highlights the Gaussianity of the posterior, with almost perfectly overlapping constraints and all the directions and widths of the Fisher ellipses recovered by the MCMC. In addition, the fiducial cosmology model values are presented with dotted black lines. They are located well within the 68% C.L. contours.

4.2. The contribution of RSD to constraining power

After we validated our MCMC pipeline, we investigated how the additional information encoded in RSD affects the constraining power on the model parameters. To do this, we considered GC alone and not the total 3×2pt because as shown in Sect. 2.2, RSD is a correction for the GC signal alone, and therefore, a change in its constraining power would be easier to appreciate. We should mention at this point that the RSD also impacts the XC part of the 3×2pt because the latter contains all the combinations of GC, WL, and XC. However, we did not perform the constraining power test due to the RSD in the 3×2pt because the WL contribution which is not affected by RSD would make the RSD impact less evident. We again focused on the w_0w_a CDM model and the pessimistic scale cut. This is reasonable because RSD mostly contributes on scales $\ell < 100$ (see Fig. 1), and therefore a higher ℓ_{\max} cut would not affect the constraining power for this test.

In particular, we compared the following two models. For the first model, we constructed the synthetic data set and covariance matrix for the photometric GC spectra including RSD (GC with RSD), and we fit it against the predictions of the w_0w_a CDM model, including RSD. The results of this analysis are shown by the orange contours in the bottom panel of Fig. 4. For the second model, we did exactly the same, but neither the synthetic data along with the covariance matrix nor the theory model included the RSD correction (GC without RSD); this corresponds to the green contours in the bottom panel of Fig. 4.

It is clear that the constraints of the two models agree very well, indicating that the RSD correction in our modelling does not add significant information on the projected cosmological parameters. This means that even though the RSD account for up to 40% of the signal for some redshift bins on the largest scales (see again top panel of Fig. 1), the cosmological information does not come from the large scales because they are dominated by cosmic variance, but gradually include smaller scales, where the RSD signal contribution becomes progressively less important.

4.3. Ignoring RSD

Regardless of the absence of an additional constraining power on cosmological parameters encoded in linear RSD, we proceeded to investigate the effect of neglecting RSD in our modelling. This investigation was performed with an MCMC analysis in Tanidis & Camera (2019), assuming a *Euclid*-like survey of intermediate-width Gaussian bins (with a photometric red-

shift scatter $0.05(1+z)$). We found that it is crucial to include RSD in the theoretical predictions to avoid biasing the cosmological parameters. This outcome of the importance of RSD in the modelling agreed with the decision in previous studies to include them in the analyses (see again the references in Sect. 1). Following the same approach, we created a mock data vector and covariance for the *Euclid* survey, with the same specifications as in EP:VII, including the RSD contribution (Sect. 2.2). The data were then analysed assuming an incorrect model without the RSD contribution. The impact of this approximation on the accuracy of the final constraints depends on the amplitude of the RSD signal, but also on the details of the experimental noise. We therefore extended the investigation of Tanidis & Camera (2019), which was only performed for GC in a Λ CDM model and in the linear regime⁴ for the density field, to more realistic settings. That is, we still considered the linear RSD, but now in the non-linear regime of the density field. In addition, we exploited photometric redshift bins from the Flagship simulation, including massive neutrinos in the analysis, and also investigated the effect on the w_0w_a CDM model. Finally, we performed the analysis both for GC alone and for the full 3×2pt, using the pessimistic and optimistic multipole cuts for both cases.

Finally, to gain better insight into the degeneracies that are present in the incorrect modelling, we recast all the final constraints on $\Omega_{m,0}$ and σ_8 in the derived parameter $S_8 = \sigma_8 \sqrt{\Omega_{m,0}/0.3}$. This parameter is particularly informative about the degenerate direction between $\Omega_{m,0}$ and σ_8 in the WL measurements that are included in the 3×2pt. However, for the sake of completeness, we calculated it for the GC alone as well.

4.3.1. Biased parameter constraints in the photometric GC

We started by obtaining constraints for both the correct (den+RSD) and incorrect models (den-only), using photometric GC alone, both assuming Λ CDM and its extension w_0w_a CDM. To assess the bias on the parameters of interest when an incorrect model is assumed, we used the relative bias which is valid for deterministic quantities assuming no stochasticity (e.g. a noiseless data vector such as we consider here),

$$B_\theta = \frac{|\theta^* - \theta^{\text{fid}}|}{\sigma_\theta}, \quad (22)$$

with θ^* being the mean estimated value on the marginalised posterior of the parameter θ , σ_θ the corresponding 68% C.L., and θ^{fid} the input fiducial value. It is defined as the offset we obtain from the input fiducial value (our benchmark) given the expected uncertainty on the parameter. Massey et al. (2012) suggested that after taking systematic effects into account, the values of $B_\theta \gtrsim 0.3$ can be considered already as statistically significant⁵.

All the Λ CDM results in GC for the correct and incorrect model, as well as the pessimistic and optimistic scale cuts, are shown in Table 3. We opted to present the incorrect model constraints for the optimistic cases alone in the top panel of Fig. 5 because the resulting biases are larger than those in the pessimistic cut. We note that in the pessimistic case, neglecting RSD leads to a bias of 4.11 and 2.69 on the parameters $\Omega_{m,0}$ and

⁴ In Tanidis & Camera (2019) only the linear matter power spectrum was used and ℓ_{\max} was defined by $k_{\max} \chi(\bar{z})$ with $k_{\max} \simeq 0.25 h \text{ Mpc}^{-1}$ and \bar{z} the mean redshift of the bin.

⁵ Values of $B_\theta < 0.3$ are considered to be permissible within the statistical fluctuation assuming that the same information for the synthetic data and the theory modelling was used.

³ we note that 68% and 95% C.L. exactly correspond to one and two standard deviations in the Gaussian approximation of the Fisher matrix after marginalising over the remaining parameters.

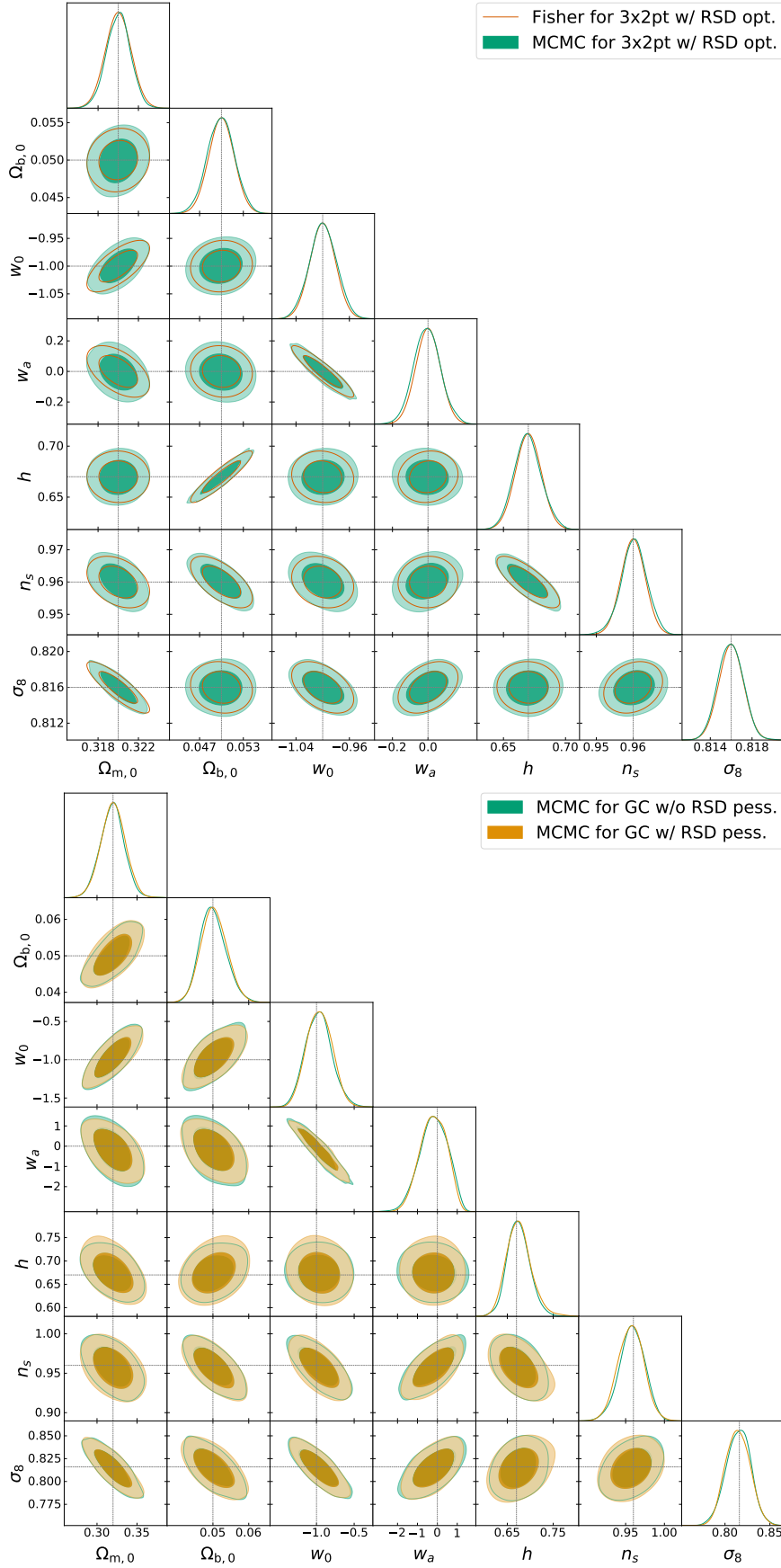


Fig. 4. 68% and 95% C.L. marginalised contours along with the one-dimensional posterior distributions on the cosmological parameters. *Top:* Constraints from the 3x2pt analysis of the flat w_0w_a CDM model for the optimistic scale cut considering RSD. The filled green contours are the MCMC constraints, and the open orange contours show the Fisher ellipses for the same modelling. The fiducial cosmology model is marked with dotted black lines. *Bottom:* Constraints from the GC alone of the flat w_0w_a CDM model (pessimistic scenario), with (orange) and without (green) RSD. The fiducial cosmology model is marked with dotted black lines.

Table 3. Summary of the mean estimated values, θ^* , along their corresponding 68% C.L. intervals, σ_θ , and the relative bias, B_θ (see Eq. 22) of a given parameter.

Parameter	Scale cut	w/ RSD			w/o RSD		
		θ^*	σ_θ	B_θ	θ^*	σ_θ	B_θ
$\Omega_{m,0}$	pess.	0.3193	0.0052	0.134	0.3019	0.0044	4.11
	opt.	0.3197	0.0037	0.08	0.3022	0.0033	5.39
$\Omega_{b,0}$	pess.	0.0503	0.0024	0.125	0.0499	0.0022	0.045
	opt.	0.0502	0.0018	0.111	0.0506	0.0018	0.33
h	pess.	0.674	0.023	0.174	0.668	0.021	0.095
	opt.	0.672	0.015	0.133	0.673	0.016	0.18
σ_8	pess.	0.8154	0.0059	0.101	0.8327	0.0062	2.69
	opt.	0.816	0.0013	0.0	0.8206	0.0013	3.53
n_s	pess.	0.96	0.012	0.0	0.959	0.011	0.091
	opt.	0.9596	0.0037	0.108	0.9684	0.0038	2.21
S_8	pess.	0.8412	0.0095	0.164	0.8353	0.009	0.829
	opt.	0.8424	0.0046	0.078	0.8236	0.0043	4.45

Note: These are the results of the GC analysis for each Λ CDM cosmological parameter for the complete (with RSD) and the incomplete (without RSD) model and for the pessimistic and optimistic scale cuts. We highlight the most biased cases ($B_\theta > 1$) with **bold**.

Table 4. Same as Table 3 for GC but for the w_0w_a CDM model.

Parameter	Scale cut	w/ RSD			w/o RSD		
		θ^*	σ_θ	B_θ	θ^*	σ_θ	B_θ
$\Omega_{m,0}$	opt.	0.3190	0.0069	0.145	0.3092	0.0056	1.928
$\Omega_{b,0}$	opt.	0.0499	0.0019	0.052	0.0516	0.0019	0.84
h	opt.	0.672	0.018	0.11	0.664	0.016	0.37
σ_8	opt.	0.8166	0.003	0.2	0.8158	0.0027	0.074
n_s	opt.	0.96	0.0043	0.0	0.9669	0.0043	1.60
w_0	opt.	-1.001	0.042	0.0238	-1.007	0.039	0.17
w_a	opt.	-0.02	0.18	0.111	0.21	0.17	1.235
S_8	opt.	0.842	0.007	0.108	0.8281	0.0058	2.52

σ_8 , respectively; while with the correct modelling we always recover the fiducial cosmology with $B_\theta \lesssim 0.3$ (see again Table 3). This bias is also imprinted on the increase in the best-fit value by $\Delta\chi^2 \approx 84.61$ with respect to the correct model.

The picture is similar for the optimistic scale cut, as the green contours in the top panel of Fig. 5 show. We note that the bias on the same parameters increases, and another mild bias now arises on n_s . In particular, the parameters $\Omega_{m,0}$, σ_8 , and n_s are biased with values 5.39, 3.53, and 2.21, respectively, and as expected there is increase in $\Delta\chi^2 \approx 92.48$ with respect to the correct model. This bias increase in the optimistic compared to the pessimistic scenario can be explained as follows: By extending the range to higher multipoles, we do not include more signal from the linear RSD which, as we saw in Sect. 2.2, contributes only on large scales ($\ell \lesssim 100$). On the other hand, we increase the constraining power on the parameters, meaning that any existing bias is enhanced by lowering the projected errors. This shows that an inaccurate modelling becomes progressively more crucial with improving data quality.

We now turn our attention on the results obtained assuming the w_0w_a CDM model. Again, we only considered the optimistic scales cut. The reason for this is that GC alone for the pessimistic scale cut is not very constraining in this model, and the bias on the parameters is expected to be small due to the smaller range of scales and the larger parameter set. The result of all this is that the w_0 and w_a parameters vary over a wide range in the MCMC, also in regions where $w_0 + w_a$ can take non-negative values (see Cepa, J. 2004, for details on the high-redshift limit of $w(z)$ in CPL). In this region of the parameter space, CAMB can-

not obtain meaningful cosmological quantities, and these points are automatically rejected from the chain, thus introducing a cut in the parameter space that is physically motivated. Based on this restriction and because the modelling for this case is not very constraining, regardless of the assumed prior on the CPL parameters, we decided to focus our analysis on the optimistic case alone. The results are shown in Table 4 and in the top panel of Fig. 5, where we still have biased estimates of our free parameters, but with a lower significance than in the Λ CDM analysis because the uncertainty brought by keeping the dark energy parameters w_0 and w_a free is larger. The parameters that are shifted by more than 1σ are $\Omega_{m,0}$, n_s , and w_a , with their B_θ values being 1.9, 1.6, and 1.2, respectively. Again, there is an increase in $\Delta\chi^2 \approx 90.65$ compared to the complete model. We summarise all the B_θ values for the aforementioned scenarios in the left panel of Fig. 6 (see the caption for details), where the trend is clearer for larger biases in the optimistic compared to the pessimistic cases and for those of the Λ CDM model against the w_0w_a CDM extension.

4.3.2. Biased parameter constraints in the 3×2pt

We repeated exactly the same analysis (different cosmologies and scale cuts) but now for the 3×2pt (Table 5, Table 6, and the bottom panel of Fig. 5). Similarly to what we saw in Sect. 4.3.1 for the Λ CDM model and the pessimistic scale cuts, the parameters $\Omega_{m,0}$, h , n_s , and σ_8 are now biased by 3.52, 3.21, 2.05, and 3.96 (see Table 5), while the overall $\Delta\chi^2$ compared to the correct model is increased by 96.27. It is interesting to note that while

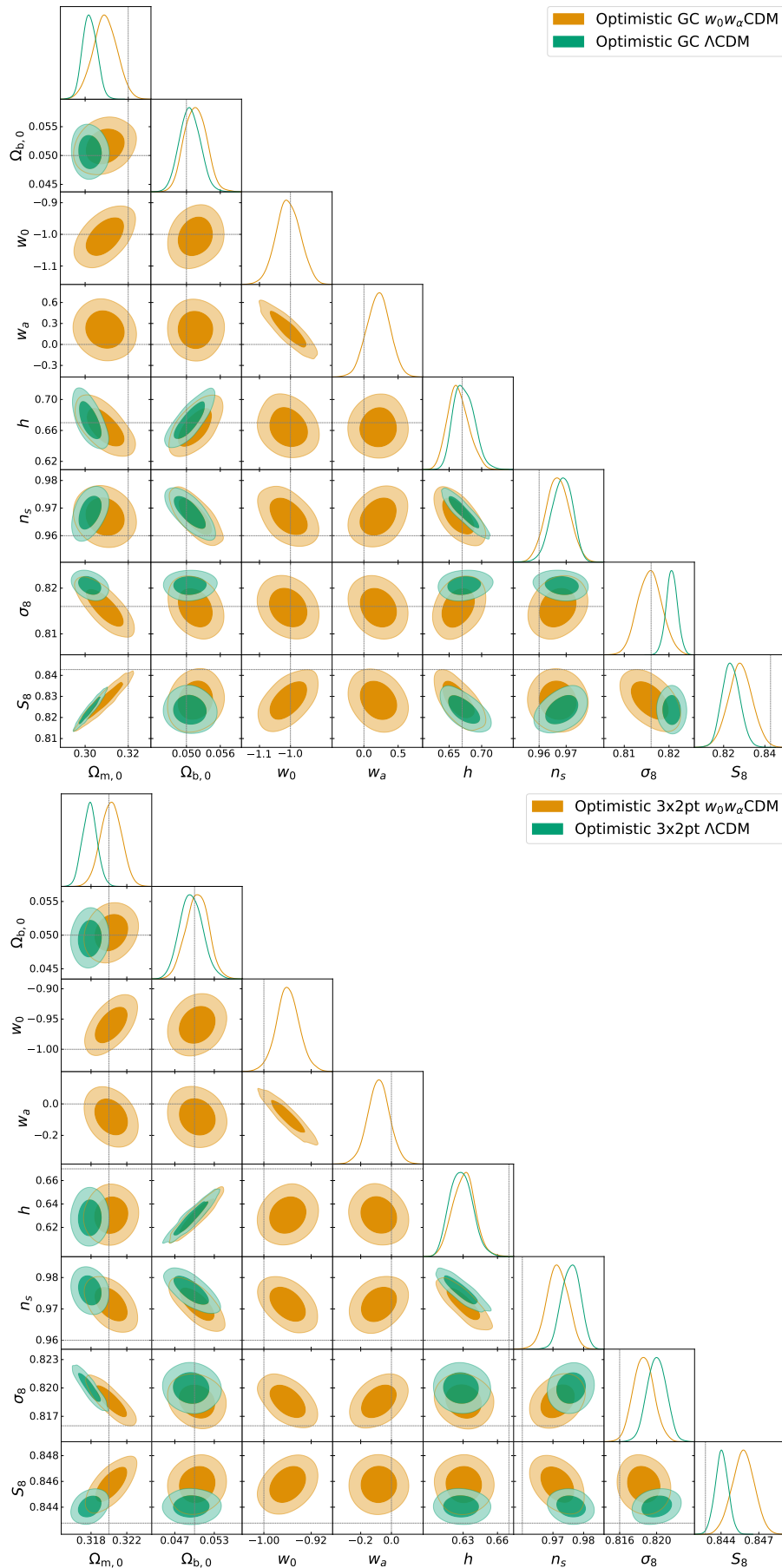


Fig. 5. 68% and 95% C.L. marginalised contours alongside the corresponding one-dimensional posterior distributions of the cosmological parameters for the incorrect modelling (without RSD). *Top:* Constraints from the GC for the ΛCDM (green contours) and $w_0w_a\text{CDM}$ model (orange contours) for the optimistic scale cut. The fiducial cosmology is marked by dotted black lines. *Bottom:* Same as above, but for 3x2pt. Article number, page 10 of 15

Table 5. Same as Table 3 but for the 3×2pt.

Parameter	scale cut	w/ RSD			w/o RSD		
		θ^*	σ_θ	B_θ	θ^*	σ_θ	B_θ
$\Omega_{m,0}$	pess.	0.32	0.0025	0.0	0.3119	0.0023	3.52
	opt.	0.32006	0.00082	0.07317	0.31786	0.00082	2.61
$\Omega_{b,0}$	pess.	0.05	0.0022	0.0	0.0481	0.002	0.95
	opt.	0.0501	0.0018	0.0555	0.0495	0.0017	0.29
h	pess.	0.671	0.016	0.062	0.625	0.014	3.21
	opt.	0.671	0.011	0.090	0.6283	0.01015	4.11
σ_8	pess.	0.816	0.0032	0.0	0.8279	0.003	3.96
	opt.	0.816	0.001	0.0	0.82	0.001	4.0
n_s	pess.	0.9596	0.0078	0.0512	0.9747	0.0072	2.05
	opt.	0.9598	0.0031	0.0645	0.9759	0.003	5.3
S_8	pess.	0.8428	0.00073	0.0531	0.84422	0.00072	2.026
	opt.	0.8428	0.00054	0.07189	0.84405	0.00052	2.478

Table 6. Same as Table 4 but for the 3×2pt.

Parameter	scale cut	w/ RSD			w/o RSD		
		θ^*	σ_θ	B_θ	θ^*	σ_θ	B_θ
$\Omega_{m,0}$	pess.	0.3202	0.0038	0.0526	0.3159	0.0035	1.17
	opt.	0.32	0.0012	0.0	0.3202	0.0012	0.16
$\Omega_{b,0}$	pess.	0.0502	0.0025	0.0799	0.0520	0.0024	0.83
	opt.	0.0499	0.0019	0.0526	0.0504	0.0017	0.23
h	pess.	0.671	0.019	0.0526	0.653	0.017	1.0
	opt.	0.67	0.01	0.0	0.6306	0.0098	4.02
σ_8	pess.	0.8158	0.0047	0.0425	0.8272	0.0044	2.54
	opt.	0.816	0.0012	0.0	0.8186	0.0011	2.36
n_s	pess.	0.9595	0.0094	0.0531	0.9557	0.0087	0.49
	opt.	0.9602	0.0035	0.0571	0.9715	0.0035	3.28
w_0	pess.	-0.9996	0.046	0.0086	-0.945	0.044	1.25
	opt.	-0.999	0.02	0.05	-0.96	0.02	2.0
w_a	pess.	0.0	0.18	0.0	0.02	0.16	0.125
	opt.	-0.005	0.075	0.066	-0.083	0.073	1.136
S_8	pess.	0.8428	0.0014	0.0277	0.8488	0.0014	4.31
	opt.	0.84273	0.00086	0.0362	0.84576	0.00089	3.37

some of the parameters (e.g. n_s and h) exhibit an increased B_θ value due to the increased constraining power of the 3×2pt combination, for the other parameters the behaviour is less straightforward. On the one hand, WL strongly constrains S_8 , which is a combination of $\Omega_{m,0}$ and σ_8 , and because this probe is not biased by neglecting RSD, we would expect a lower bias for these parameters. On the other hand, however, the inclusion of XC lifts the degeneracy between σ_8 and the bias parameters present in the GC probe, thus making the latter more sensitive to this parameter. Because both GC and XC are biased when we neglect RSD, the overall effect is an increased B_θ value on σ_8 with respect to the case of GC alone.

In the optimistic case, the balance between these effects changes because the increased number of scales available for WL makes this more relevant, thus reducing the bias with respect to the case of GC alone. This does not apply to n_s and h , which are still mostly constrained by GC. The $\Delta\chi^2$ is increased by 106.78 with respect to the correct model.

Finally, the results of the 3×2pt and the w_0w_a CDM model are shown in Table 6. In the pessimistic case, the biased estimate for σ_8 is 2.54, and the peaks for the parameters $\Omega_{m,0}$, $\Omega_{b,0}$, w_0 , and h are misplaced with biases of 1.17, 0.83, 1.25, and 1.00, while for the optimistic scenario (see again Table 6 and the orange contours in the bottom panel of Fig. 5), there are biased estimates for w_0 , w_a , h , n_s , and σ_8 at 2.00, 1.14, 4.02, 3.28, and 2.36, respec-

tively. Both models yield an increased $\Delta\chi^2$ compared to the complete model by 92.05 (pessimistic) and 103.6 (optimistic). When the latter case is compared to GC alone, the increased constraining power, brought by WL and XC, has the effect of increasing the significance of the bias on most of the parameters. Similarly to Sect. 4.3.1, we summarise the B_θ values for all the cases of the 3×2pt in the right panel of Fig. 6.

5. Conclusions

In this work, we have aimed to quantify the contribution of linear RSD in photometric GC as is expected to be measured by *Euclid*, both as a stand-alone probe and in combination with cosmic shear (WL), in the so-called 3×2pt approach. We followed Tanidis & Camera (2019) and included RSD in the angular power spectra of GC and its cross-correlation with WL (XC).

Using the galaxy distribution information coming from the Flagship simulation, and the *Euclid* specifications discussed in EP:VII, we generated synthetic data by generating angular power spectra and covariance matrix with a fiducial cosmology, for the photometric observations of *Euclid* and produced the posterior distributions for the free parameters of our model in an MCMC framework.

As a first step, we validated our results against a Fisher matrix approach and found that they agree very well. Then, we com-

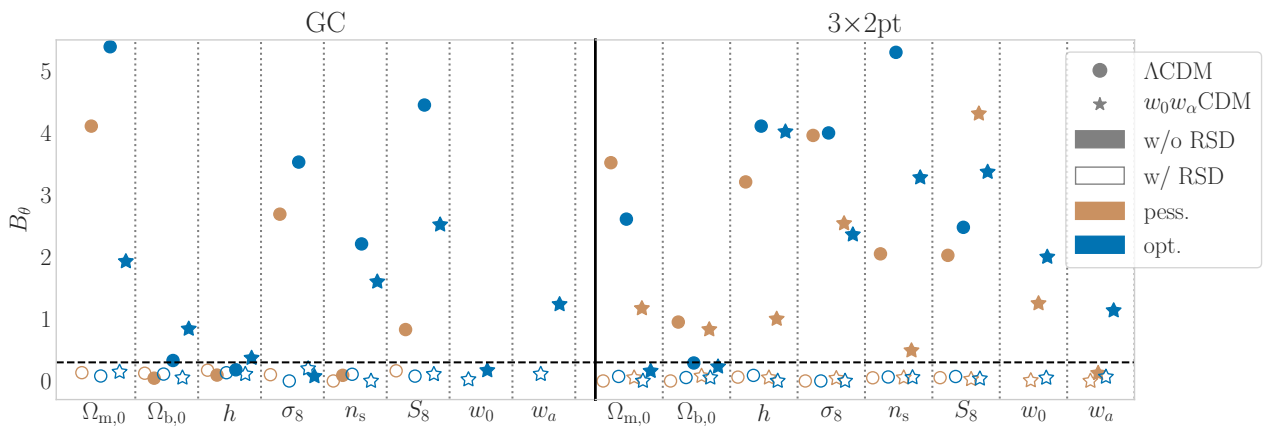


Fig. 6. Summary plot of the B_θ values for the GC (left) and the $3\times 2\text{pt}$ (right) for all the examined cases. The circles correspond to the ΛCDM cosmology model and the stars show the $w_0 w_a \text{CDM}$ extension. The open and filled symbols show a theory modelling with and without RSD, respectively. The pessimistic and optimistic scale cuts are shown in brown and blue. The horizontal dashed line denotes the value $B_\theta = 0.3$

pared the constraints on the cosmological parameters that are obtained when the theoretical predictions are computed with the contribution of RSD to those obtained when RSD are neglected. When GC is used as a stand-alone probe and a ΛCDM cosmology is assumed for the theoretical predictions, neglecting RSD can lead to significant inaccuracies on the reconstruction of cosmological parameters, in particular, in the most optimistic case when the constraining power of our experimental setup is maximum. We find that the parameters $\Omega_{m,0}$, n_s , and σ_8 are all significantly shifted from their (input) fiducial values with biases of 5.4σ , 2.2σ , and 3.5σ , respectively. The statistical significance of these shifts is reduced when the cosmological model used to fit the data allows the w_0 and w_a parameters to take values different from ΛCDM , however. The inclusion of these two additional parameters degrades the constraining power and leads to a less evident shift than in the fiducial model.

We included WL and XC in the analysis to perform a $3\times 2\text{pt}$ analysis. In this case, we found a non-trivial effect on the significance of the RSD contribution. On the one hand, WL contributes to tighten the constraints that can be achieved with *Euclid*, thus potentially increasing the significance of the shifts that are obtained when RSD is neglected. On the other hand, the theoretical predictions for this probe are not biased by this approximation (although the XC is still biased), and the inclusion of WL can therefore drag the recovered posterior distribution towards the fiducial values even when RSD are neglected. We found that for parameters such as n_s and h , where galaxy GC dominate, WL simply improve the constraining power, and the bias on these parameters increases in significance. In contrast, the parameters that are mostly constrained by WL, such as $\Omega_{m,0}$ and σ_8 , we found that their shifts decrease in the optimistic case, where the constraining power of WL dominates the constraining power from GC.

To summarise, we found that when the contribution of linear RSD is not included in the theoretical predictions for GC angular power spectra, it can significantly reduce the accuracy but not the precision of the constraints that can be achieved by *Euclid*. The reason is that the linear RSD contribute at scales $\ell < 100$, which is a cosmic-variance dominated regime that yields no gain in cosmological information. It is important to note that the necessity of including the effect of linear RSD in GC in order to avoid cosmology biases has been studied in depth (Scharf et al. 1994; Heavens & Taylor 1995; Padmanabhan et al. 2007; Blake

et al. 2007; Nock et al. 2010; Crocce et al. 2011; Balaguera-Antolínez et al. 2018; Abbott et al. 2022) and the findings of our work agree with this. However, we have demonstrated that the approach of Tanidis & Camera (2019), which is a fast and approximated way to account for the linear RSD correction, can easily be implemented and tested within a parameter estimation pipeline in the modelling of *Euclid* photometric observables. In addition to this, work is ongoing to improve the modelling and study the effect of the non-linear galaxy bias in the photometric GC, which becomes especially important for Stage-IV galaxy surveys such as *Euclid*.

Acknowledgements. KT is supported by the STFC grant ST/W000903/1 and by the European Structural and Investment Fund. For most of the development of this project KT was supported by the Czech Ministry of Education, Youth and Sports (Project CoGraDS - CZ.02.1.01/0.0/0.0/15_003/0000437). V.C and M.M. acknowledge funding by the Agenzia Spaziale Italiana (ASI) under agreement no. 2018-23-HH.0 and support from INFN/Euclid Sezione di Roma. IT acknowledges funding from the European Research Council (ERC) under the European Union’s Horizon 2020 research and innovation programme (Grant agreement No. 863929; project title “Testing the law of gravity with novel large-scale structure observables”). SC acknowledges support from the ‘Departments of Excellence 2018-2022’ Grant (L. 232/2016) awarded by the Italian Ministry of University and Research (MUR). The Euclid Consortium acknowledges the European Space Agency and a number of agencies and institutes that have supported the development of *Euclid*, in particular the Academy of Finland, the Agenzia Spaziale Italiana, the Belgian Science Policy, the Canadian Euclid Consortium, the French Centre National d’Etudes Spatiales, the Deutsches Zentrum für Luft- und Raumfahrt, the Danish Space Research Institute, the Fundação para a Ciência e a Tecnologia, the Ministerio de Ciencia e Innovación, the National Aeronautics and Space Administration, the National Astronomical Observatory of Japan, the Nederlandse Onderzoekschool Voor Astronomie, the Norwegian Space Agency, the Romanian Space Agency, the State Secretariat for Education, Research and Innovation (SERI) at the Swiss Space Office (SSO), and the United Kingdom Space Agency. A complete and detailed list is available on the *Euclid* web site (<http://www.euclid-ec.org>).

References

- Abbott, T. M. C., Abdalla, F. B., Annis, J., et al. 2018, *MNRAS*, 480, 3879
 Abbott, T. M. C., Aguena, M., Alarcon, A., et al. 2022, *Phys. Rev. D*, 105, 023520
 Abdalla, F. B., Bull, P., Camera, S., et al. 2015, in *Advancing Astrophysics with the Square Kilometre Array (AASKA14)*, 17
 Alsing, J., Kirk, D., Heavens, A., & Jaffe, A. H. 2015, *MNRAS*, 452, 1202
 Amendola, L., Appleby, S., Avgoustidis, A., et al. 2018, *Living Rev. Rel.*, 21, 2
 Amendola, L., Appleby, S., Bacon, D., et al. 2013, *Living Rev. Rel.*, 16, 6
 Andrade-Oliveira, F., Camacho, H., Faga, L., et al. 2021, *MNRAS*, 505, 5714
 Balaguera-Antolínez, A., Bilicki, M., & Branchini, E. 2018, *MNRAS*, 476, 1050

- Behroozi, P. S., Wechsler, R. H., & Wu, H.-Y. 2013, *ApJ*, 762, 109
- Bird, S., Viel, M., & Haehnelt, M. G. 2012, *MNRAS*, 420, 2551
- Blake, C., Collister, A., & Bridle, S. 2007, *MNRAS*, 374, 1527
- Blanton, M. R., Hogg, D. W., Bahcall, N. A., et al. 2003, *ApJ*, 594, 186
- Blanton, M. R., Lupton, R. H., Schlegel, D. J., et al. 2005, *ApJ*, 631, 208
- Blanton, M. R., Schlegel, D. J., Strauss, M. A., et al. 2005, *AJ*, 129, 2562
- Bonvin, C. & Durrer, R. 2011, *Phys. Rev.*, D84, 063505
- Brown, M., Bacon, D., Camera, S., et al. 2015, in *Advancing Astrophysics with the Square Kilometre Array (AASKA14)*, 23
- Bull, P., Camera, S., Raccanelli, A., et al. 2015, in *Advancing Astrophysics with the Square Kilometre Array (AASKA14)*, 24
- Camera, S., Maartens, R., & Santos, M. G. 2015a, *MNRAS*, 451, L80
- Camera, S., Raccanelli, A., Bull, P., et al. 2015b, in *Advancing Astrophysics with the Square Kilometre Array (AASKA14)*, 25
- Carretero, J., Castander, F. J., Gaztañaga, E., Crocce, M., & Fosalba, P. 2015, *MNRAS*, 447, 646
- Cepa, J. 2004, *A&A*, 422, 831
- Challinor, A. & Lewis, A. 2011, *Phys. Rev.*, D84, 043516
- Chevallier & Polarski. 2001, *International Journal of Modern Physics D*, 10, 213
- Costille, A., Caillat, A., Rossin, C., et al. 2018, in *Space Telescopes and Instrumentation 2018: Optical, Infrared, and Millimeter Wave*, ed. M. Lystrup, H. A. MacEwen, G. G. Fazio, N. Batalha, N. Siegler, & E. C. Tong, Vol. 10698, *International Society for Optics and Photonics (SPIE)*, 730
- Crocce, M., Cabré, A., & Gaztañaga, E. 2011, *MNRAS*, 414, 329
- Cropper, M., Pottinger, S., Azzollini, R., et al. 2018, in *Space Telescopes and Instrumentation 2018: Optical, Infrared, and Millimeter Wave*, ed. M. Lystrup, H. A. MacEwen, G. G. Fazio, N. Batalha, N. Siegler, & E. C. Tong, Vol. 10698, *International Society for Optics and Photonics (SPIE)*, 709
- De Vicente, J., Sánchez, E., & Sevilla-Noarbe, I. 2016, *MNRAS*, 459, 3078
- DES Collaboration: Abbott, T., Aldering, G., Annis, J., et al. 2005 [arXiv:astro-ph/0510346]
- DESI Collaboration: Aghamousa, A., Aguilar, J., Ahlen, S., et al. 2016a [arXiv:1611.00036]
- DESI Collaboration: Aghamousa, A., Aguilar, J., Ahlen, S., et al. 2016b [arXiv:1611.00037]
- Desjacques, V., Jeong, D., & Schmidt, F. 2018, *Physics Reports*, 733, 1
- Doré, O., Bock, J., Ashby, M., et al. 2014 [arXiv:1412.4872]
- Doré, O., Werner, M. W., Ashby, M. L. N., et al. 2018 [arXiv:1805.05489]
- Elvin-Poole, J., Crocce, M., Ross, A. J., et al. 2018, *Phys. Rev.*, D98, 042006
- Euclid Collaboration: Ajani, V., Baldi, M., Barthelemy, A., et al. 2023, *A&A*, 675, A120
- Euclid Collaboration: Blanchard, A., Camera, S., Carbone, C., et al. 2020, *A&A*, 642, A191
- Euclid Collaboration: Pocino, A., Tutusaus, I., Castander, F. J., et al. 2021, *A&A*, 655, A44
- Foreman-Mackey, D., Hogg, D. W., Lang, D., & Goodman, J. 2013, *Publ. Astron. Soc. Pac.*, 125, 306
- Heavens, A., Alsing, J., & Jaffe, A. H. 2013, *MNRAS*, 433, L6
- Heavens, A. F. & Taylor, A. N. 1995, *MNRAS*, 275, 483
- Howlett, C., Lewis, A., Hall, A., & Challinor, A. 2012, *JCAP*, 2012, 027
- Ivezic, v., Kahn, S. M., Tyson, A. J., et al. 2019, *ApJ*, 873, 111
- Joachimi, B., Cacciato, M., Kitching, T. D., et al. 2015, *Space Science Reviews*, 193, 1
- Kaiser, N. 1987, *MNRAS*, 227, 1
- Kaiser, N. 1992, *ApJ*, 388, 272
- Laureijs, R., Amiaux, J., Arduini, S., et al. 2011 [arXiv:1110.3193]
- Lepori, F., Tutusaus, I., Viglione, C., et al. 2022, *A&A*, 662, A93
- Lewis, A., Challinor, A., & Lasenby, A. 2000, *ApJ*, 538, 473
- Linder, E. V. 2003, *Phys. Rev. Lett.*, 90, 091301
- LSST Dark Energy Science Collaboration: Mandelbaum, R., Eifler, T., Hložek, R., et al. 2018 [arXiv:1809.01669]
- LSST Science Collaboration: Abell, P., A., Allison, J., Anderson, S., F., et al. 2009 [arXiv:0912.0201]
- Martinelli, M., Dalal, R., Majidi, F., et al. 2022, *MNRAS*, 510, 1964
- Massey, R., Hoekstra, H., Kitching, T., et al. 2012, *MNRAS*, 429, 661
- Nock, K., Percival, W. J., & Ross, A. J. 2010, *MNRAS*, 407, 520
- Padmanabhan, N., Schlegel, D. J., Seljak, U., et al. 2007, *MNRAS*, 378, 852
- Potter, D., Stadel, J., & Teyssier, R. 2017, *Computational Astrophysics and Cosmology*, 4, 2
- Raccanelli, A., Bull, P., Camera, S., et al. 2015, in *Advancing Astrophysics with the Square Kilometre Array (AASKA14)*, 31
- Santos, M., Bull, P., Alonso, D., et al. 2015, in *Advancing Astrophysics with the Square Kilometre Array (AASKA14)*, 19
- Scharf, C. A., Fisher, K. B., & Lahav, O. 1994, *MNRAS*, 266, 219
- Schneider, P., Eifler, T., & Krause, E. 2010, *A&A*, 520, A116
- SKA Cosmology Science Working Group. 2020, *PASA*, 37, e007
- Smith, R. E., Peacock, J. A., Jenkins, A., et al. 2003, *MNRAS*, 341, 1311
- Spergel, D., Gehrels, N., Baltay, C., et al. 2015 [arXiv:1503.03757]
- Szalay, A. S., Matsubara, T., & Landy, S. D. 1998, *ApJ*, 498, L1
- Sánchez, A. G., Scoccimarro, R., Crocce, M., et al. 2016, *MNRAS*, 464, 1640
- Takahashi, R., Sato, M., Nishimichi, T., Taruya, A., & Oguri, M. 2012, *ApJ*, 761, 152
- Tanidis, K. & Camera, S. 2019, *MNRAS*, 489, 3385
- Tanidis, K., Camera, S., & Parkinson, D. 2019, *MNRAS*, 491, 4869
- Yoo, J. 2010, *Phys. Rev.*, D82, 083508
- Zehavi, I., Zheng, Z., Weinberg, D. H., et al. 2011, *ApJ*, 736, 59
- Zuntz, J., Paterno, M., Jennings, E., et al. 2015, *Astron. Comput.*, 12, 45
- ¹ CEICO, Institute of Physics of the Czech Academy of Sciences, Na Slovance 2, Praha 8, Czech Republic
- ² Department of Physics, Oxford University, Keble Road, Oxford OX1 3RH, UK
- ³ INAF-Osservatorio Astronomico di Roma, Via Frascati 33, 00078 Monteporzio Catone, Italy
- ⁴ INFN-Sezione di Roma, Piazzale Aldo Moro, 2 - c/o Dipartimento di Fisica, Edificio G. Marconi, 00185 Roma, Italy
- ⁵ Institut de Recherche en Astrophysique et Planétologie (IRAP), Université de Toulouse, CNRS, UPS, CNES, 14 Av. Edouard Belin, 31400 Toulouse, France
- ⁶ Université de Genève, Département de Physique Théorique and Centre for Astroparticle Physics, 24 quai Ernest-Ansermet, CH-1211 Genève 4, Switzerland
- ⁷ Dipartimento di Fisica, Università degli Studi di Torino, Via P. Giuria 1, 10125 Torino, Italy
- ⁸ INFN-Sezione di Torino, Via P. Giuria 1, 10125 Torino, Italy
- ⁹ INAF-Osservatorio Astrofisico di Torino, Via Osservatorio 20, 10025 Pino Torinese (TO), Italy
- ¹⁰ Université Paris-Saclay, CNRS, Institut d'astrophysique spatiale, 91405, Orsay, France
- ¹¹ Institute of Cosmology and Gravitation, University of Portsmouth, Portsmouth PO1 3FX, UK
- ¹² INAF-Osservatorio Astronomico di Brera, Via Brera 28, 20122 Milano, Italy
- ¹³ INAF-Osservatorio di Astrofisica e Scienza dello Spazio di Bologna, Via Piero Gobetti 93/3, 40129 Bologna, Italy
- ¹⁴ Dipartimento di Fisica e Astronomia, Università di Bologna, Via Gobetti 93/2, 40129 Bologna, Italy
- ¹⁵ INFN-Sezione di Bologna, Viale Berti Pichat 6/2, 40127 Bologna, Italy
- ¹⁶ Dipartimento di Fisica, Università di Genova, Via Dodecaneso 33, 16146, Genova, Italy
- ¹⁷ INFN-Sezione di Genova, Via Dodecaneso 33, 16146, Genova, Italy
- ¹⁸ Department of Physics "E. Pancini", University Federico II, Via Cinthia 6, 80126, Napoli, Italy
- ¹⁹ INAF-Osservatorio Astronomico di Capodimonte, Via Moiariello 16, 80131 Napoli, Italy
- ²⁰ Instituto de Astrofísica e Ciências do Espaço, Universidade do Porto, CAUP, Rua das Estrelas, PT4150-762 Porto, Portugal
- ²¹ INAF-IASF Milano, Via Alfonso Corti 12, 20133 Milano, Italy
- ²² Institut de Física d'Altes Energies (IFAE), The Barcelona Institute of Science and Technology, Campus UAB, 08193 Bellaterra (Barcelona), Spain
- ²³ Port d'Informació Científica, Campus UAB, C. Albareda s/n, 08193 Bellaterra (Barcelona), Spain
- ²⁴ Institute for Theoretical Particle Physics and Cosmology (TTK), RWTH Aachen University, 52056 Aachen, Germany
- ²⁵ INFN section of Naples, Via Cinthia 6, 80126, Napoli, Italy
- ²⁶ Dipartimento di Fisica e Astronomia "Augusto Righi" - Alma Mater Studiorum Università di Bologna, Viale Berti Pichat 6/2, 40127 Bologna, Italy
- ²⁷ Centre National d'Etudes Spatiales – Centre spatial de Toulouse, 18 avenue Edouard Belin, 31401 Toulouse Cedex 9, France
- ²⁸ Institut national de physique nucléaire et de physique des particules, 3 rue Michel-Ange, 75794 Paris Cédex 16, France
- ²⁹ Institute for Astronomy, University of Edinburgh, Royal Observatory, Blackford Hill, Edinburgh EH9 3HJ, UK
- ³⁰ European Space Agency/ESRIN, Largo Galileo Galilei 1, 00044 Frascati, Roma, Italy
- ³¹ ESAC/ESA, Camino Bajo del Castillo, s/n., Urb. Villafranca del Castillo, 28692 Villanueva de la Cañada, Madrid, Spain

- ³² University of Lyon, Univ Claude Bernard Lyon 1, CNRS/IN2P3, IP2I Lyon, UMR 5822, 69622 Villeurbanne, France
- ³³ Institute of Physics, Laboratory of Astrophysics, Ecole Polytechnique Fédérale de Lausanne (EPFL), Observatoire de Sauverny, 1290 Versoix, Switzerland
- ³⁴ UCB Lyon 1, CNRS/IN2P3, IUF, IP2I Lyon, 4 rue Enrico Fermi, 69622 Villeurbanne, France
- ³⁵ Departamento de Física, Faculdade de Ciências, Universidade de Lisboa, Edifício C8, Campo Grande, PT1749-016 Lisboa, Portugal
- ³⁶ Instituto de Astrofísica e Ciências do Espaço, Faculdade de Ciências, Universidade de Lisboa, Campo Grande, 1749-016 Lisboa, Portugal
- ³⁷ Department of Astronomy, University of Geneva, ch. d'Ecogia 16, 1290 Versoix, Switzerland
- ³⁸ INFN-Padova, Via Marzolo 8, 35131 Padova, Italy
- ³⁹ INAF-Istituto di Astrofisica e Planetologia Spaziali, via del Fosso del Cavaliere, 100, 00100 Roma, Italy
- ⁴⁰ Université Paris-Saclay, Université Paris Cité, CEA, CNRS, AIM, 91191, Gif-sur-Yvette, France
- ⁴¹ Institute of Space Sciences (ICE, CSIC), Campus UAB, Carrer de Can Magrans, s/n, 08193 Barcelona, Spain
- ⁴² Institut d'Estudis Espacials de Catalunya (IEEC), Carrer Gran Capitá 2-4, 08034 Barcelona, Spain
- ⁴³ INAF-Osservatorio Astronomico di Trieste, Via G. B. Tiepolo 11, 34143 Trieste, Italy
- ⁴⁴ Aix-Marseille Université, CNRS/IN2P3, CPPM, Marseille, France
- ⁴⁵ INAF-Osservatorio Astronomico di Padova, Via dell'Osservatorio 5, 35122 Padova, Italy
- ⁴⁶ Max Planck Institute for Extraterrestrial Physics, Giessenbachstr. 1, 85748 Garching, Germany
- ⁴⁷ University Observatory, Faculty of Physics, Ludwig-Maximilians-Universität, Scheinerstr. 1, 81679 Munich, Germany
- ⁴⁸ Dipartimento di Fisica "Aldo Pontremoli", Università degli Studi di Milano, Via Celoria 16, 20133 Milano, Italy
- ⁴⁹ INFN-Sezione di Milano, Via Celoria 16, 20133 Milano, Italy
- ⁵⁰ Institute of Theoretical Astrophysics, University of Oslo, P.O. Box 1029 Blindern, 0315 Oslo, Norway
- ⁵¹ Jet Propulsion Laboratory, California Institute of Technology, 4800 Oak Grove Drive, Pasadena, CA, 91109, USA
- ⁵² Department of Physics, Lancaster University, Lancaster, LA1 4YB, UK
- ⁵³ Technical University of Denmark, Elektrovej 327, 2800 Kgs. Lyngby, Denmark
- ⁵⁴ Cosmic Dawn Center (DAWN), Denmark
- ⁵⁵ Max-Planck-Institut für Astronomie, Königstuhl 17, 69117 Heidelberg, Germany
- ⁵⁶ Department of Physics and Astronomy, University College London, Gower Street, London WC1E 6BT, UK
- ⁵⁷ Department of Physics and Helsinki Institute of Physics, Gustaf Hällströmin katu 2, 00014 University of Helsinki, Finland
- ⁵⁸ Department of Physics, P.O. Box 64, 00014 University of Helsinki, Finland
- ⁵⁹ Helsinki Institute of Physics, Gustaf Hällströmin katu 2, University of Helsinki, Helsinki, Finland
- ⁶⁰ NOVA optical infrared instrumentation group at ASTRON, Oude Hoogeveensedijk 4, 7991PD, Dwingeloo, The Netherlands
- ⁶¹ Universität Bonn, Argelander-Institut für Astronomie, Auf dem Hügel 71, 53121 Bonn, Germany
- ⁶² Aix-Marseille Université, CNRS, CNES, LAM, Marseille, France
- ⁶³ Dipartimento di Fisica e Astronomia "Augusto Righi" - Alma Mater Studiorum Università di Bologna, via Piero Gobetti 93/2, 40129 Bologna, Italy
- ⁶⁴ Department of Physics, Institute for Computational Cosmology, Durham University, South Road, DH1 3LE, UK
- ⁶⁵ Université Côte d'Azur, Observatoire de la Côte d'Azur, CNRS, Laboratoire Lagrange, Bd de l'Observatoire, CS 34229, 06304 Nice cedex 4, France
- ⁶⁶ Université Paris Cité, CNRS, Astroparticule et Cosmologie, 75013 Paris, France
- ⁶⁷ European Space Agency/ESTEC, Keplerlaan 1, 2201 AZ Noordwijk, The Netherlands
- ⁶⁸ Department of Physics and Astronomy, University of Aarhus, Ny Munkegade 120, DK-8000 Aarhus C, Denmark
- ⁶⁹ Centre for Astrophysics, University of Waterloo, Waterloo, Ontario N2L 3G1, Canada
- ⁷⁰ Department of Physics and Astronomy, University of Waterloo, Waterloo, Ontario N2L 3G1, Canada
- ⁷¹ Perimeter Institute for Theoretical Physics, Waterloo, Ontario N2L 2Y5, Canada
- ⁷² Université Paris-Saclay, Université Paris Cité, CEA, CNRS, Astrophysique, Instrumentation et Modélisation Paris-Saclay, 91191 Gif-sur-Yvette, France
- ⁷³ Space Science Data Center, Italian Space Agency, via del Politecnico snc, 00133 Roma, Italy
- ⁷⁴ CEA Saclay, DFR/IRFU, Service d'Astrophysique, Bat. 709, 91191 Gif-sur-Yvette, France
- ⁷⁵ Institute of Space Science, Str. Atomistilor, nr. 409 Măgurele, Ilfov, 077125, Romania
- ⁷⁶ Dipartimento di Fisica e Astronomia "G. Galilei", Università di Padova, Via Marzolo 8, 35131 Padova, Italy
- ⁷⁷ Universitäts-Sternwarte München, Fakultät für Physik, Ludwig-Maximilians-Universität München, Scheinerstrasse 1, 81679 München, Germany
- ⁷⁸ Departamento de Física, FCFM, Universidad de Chile, Blanco Encalada 2008, Santiago, Chile
- ⁷⁹ Atlantis, University Science Park, Sede Bld 48940, Leioa-Bilbao, Spain
- ⁸⁰ Centro de Investigaciones Energéticas, Medioambientales y Tecnológicas (CIEMAT), Avenida Complutense 40, 28040 Madrid, Spain
- ⁸¹ Instituto de Astrofísica e Ciências do Espaço, Faculdade de Ciências, Universidade de Lisboa, Tapada da Ajuda, 1349-018 Lisboa, Portugal
- ⁸² Universidad Politécnica de Cartagena, Departamento de Electrónica y Tecnología de Computadoras, Plaza del Hospital 1, 30202 Cartagena, Spain
- ⁸³ Kapteyn Astronomical Institute, University of Groningen, PO Box 800, 9700 AV Groningen, The Netherlands
- ⁸⁴ INFN-Bologna, Via Irnerio 46, 40126 Bologna, Italy
- ⁸⁵ Infrared Processing and Analysis Center, California Institute of Technology, Pasadena, CA 91125, USA
- ⁸⁶ IFPU, Institute for Fundamental Physics of the Universe, via Beirut 2, 34151 Trieste, Italy
- ⁸⁷ Instituto de Astrofísica de Canarias, Calle Vía Láctea s/n, 38204, San Cristóbal de La Laguna, Tenerife, Spain
- ⁸⁸ University of Applied Sciences and Arts of Northwestern Switzerland, School of Engineering, 5210 Windisch, Switzerland
- ⁸⁹ Institut d'Astrophysique de Paris, 98bis Boulevard Arago, 75014, Paris, France
- ⁹⁰ Junia, EPA department, 41 Bd Vauban, 59800 Lille, France
- ⁹¹ Instituto de Física Teórica UAM-CSIC, Campus de Cantoblanco, 28049 Madrid, Spain
- ⁹² CERCA/ISO, Department of Physics, Case Western Reserve University, 10900 Euclid Avenue, Cleveland, OH 44106, USA
- ⁹³ Laboratoire de Physique de l'École Normale Supérieure, ENS, Université PSL, CNRS, Sorbonne Université, 75005 Paris, France
- ⁹⁴ Observatoire de Paris, Université PSL, Sorbonne Université, LERMA, 750 Paris, France
- ⁹⁵ Astrophysics Group, Blackett Laboratory, Imperial College London, London SW7 2AZ, UK
- ⁹⁶ Scuola Normale Superiore, Piazza dei Cavalieri 7, 56126 Pisa, Italy
- ⁹⁷ SISSA, International School for Advanced Studies, Via Bonomea 265, 34136 Trieste TS, Italy
- ⁹⁸ INFN, Sezione di Trieste, Via Valerio 2, 34127 Trieste TS, Italy
- ⁹⁹ Departamento de Astrofísica, Universidad de La Laguna, 38206, La Laguna, Tenerife, Spain
- ¹⁰⁰ Dipartimento di Fisica e Scienze della Terra, Università degli Studi di Ferrara, Via Giuseppe Saragat 1, 44122 Ferrara, Italy
- ¹⁰¹ Istituto Nazionale di Fisica Nucleare, Sezione di Ferrara, Via Giuseppe Saragat 1, 44122 Ferrara, Italy
- ¹⁰² Institut de Physique Théorique, CEA, CNRS, Université Paris-Saclay 91191 Gif-sur-Yvette Cedex, France
- ¹⁰³ Institut d'Astrophysique de Paris, UMR 7095, CNRS, and Sorbonne

Université, 98 bis boulevard Arago, 75014 Paris, France

¹⁰⁴ Dipartimento di Fisica - Sezione di Astronomia, Università di Trieste, Via Tiepolo 11, 34131 Trieste, Italy

¹⁰⁵ NASA Ames Research Center, Moffett Field, CA 94035, USA

¹⁰⁶ Kavli Institute for Particle Astrophysics & Cosmology (KIPAC), Stanford University, Stanford, CA 94305, USA

¹⁰⁷ INAF, Istituto di Radioastronomia, Via Piero Gobetti 101, 40129 Bologna, Italy

¹⁰⁸ Institute Lorentz, Leiden University, PO Box 9506, Leiden 2300 RA, The Netherlands

¹⁰⁹ Institute for Astronomy, University of Hawaii, 2680 Woodlawn Drive, Honolulu, HI 96822, USA

¹¹⁰ Department of Physics & Astronomy, University of California Irvine, Irvine CA 92697, USA

¹¹¹ Departamento Física Aplicada, Universidad Politécnica de Cartagena, Campus Muralla del Mar, 30202 Cartagena, Murcia, Spain

¹¹² Department of Astronomy & Physics and Institute for Computational Astrophysics, Saint Mary's University, 923 Robie Street, Halifax, Nova Scotia, B3H 3C3, Canada

¹¹³ Dipartimento di Fisica, Università degli studi di Genova, and INFN-Sezione di Genova, via Dodecaneso 33, 16146, Genova, Italy

¹¹⁴ Department of Computer Science, Aalto University, PO Box 15400, Espoo, FI-00 076, Finland

¹¹⁵ Ruhr University Bochum, Faculty of Physics and Astronomy, Astronomical Institute (AIRUB), German Centre for Cosmological Lensing (GCCL), 44780 Bochum, Germany

¹¹⁶ Université Paris-Saclay, CNRS/IN2P3, IJCLab, 91405 Orsay, France

¹¹⁷ Department of Physics and Astronomy, Vesilinnantie 5, 20014 University of Turku, Finland

¹¹⁸ Serco for European Space Agency (ESA), Camino bajo del Castillo, s/n, Urbanización Villafranca del Castillo, Villanueva de la Cañada, 28692 Madrid, Spain

¹¹⁹ AIM, CEA, CNRS, Université Paris-Saclay, Université de Paris, 91191 Gif-sur-Yvette, France

¹²⁰ Oskar Klein Centre for Cosmoparticle Physics, Department of Physics, Stockholm University, Stockholm, SE-106 91, Sweden

¹²¹ Univ. Grenoble Alpes, CNRS, Grenoble INP, LPSC-IN2P3, 53, Avenue des Martyrs, 38000, Grenoble, France

¹²² Centre de Calcul de l'IN2P3/CNRS, 21 avenue Pierre de Coubertin 69627 Villeurbanne Cedex, France

¹²³ Dipartimento di Fisica, Sapienza Università di Roma, Piazzale Aldo Moro 2, 00185 Roma, Italy

¹²⁴ Centro de Astrofísica da Universidade do Porto, Rua das Estrelas, 4150-762 Porto, Portugal

¹²⁵ Dipartimento di Fisica, Università di Roma Tor Vergata, Via della Ricerca Scientifica 1, Roma, Italy

¹²⁶ INFN, Sezione di Roma 2, Via della Ricerca Scientifica 1, Roma, Italy

¹²⁷ Department of Mathematics and Physics E. De Giorgi, University of Salento, Via per Arnesano, CP-193, 73100, Lecce, Italy

¹²⁸ INAF-Sezione di Lecce, c/o Dipartimento Matematica e Fisica, Via per Arnesano, 73100, Lecce, Italy

¹²⁹ INFN, Sezione di Lecce, Via per Arnesano, CP-193, 73100, Lecce, Italy

¹³⁰ Institute for Computational Science, University of Zurich, Winterthurerstrasse 190, 8057 Zurich, Switzerland

¹³¹ Institut für Theoretische Physik, University of Heidelberg, Philosophenweg 16, 69120 Heidelberg, Germany

¹³² Université St Joseph; Faculty of Sciences, Beirut, Lebanon

¹³³ Mullard Space Science Laboratory, University College London, Holmbury St Mary, Dorking, Surrey RH5 6NT, UK

¹³⁴ Department of Astrophysical Sciences, Peyton Hall, Princeton University, Princeton, NJ 08544, USA

¹³⁵ Niels Bohr Institute, University of Copenhagen, Jagtvej 128, 2200 Copenhagen, Denmark

¹³⁶ Cosmic Dawn Center (DAWN)

¹³⁷ Universität Innsbruck, Institut für Astro- und Teilchenphysik, Technikerstr. 25/8, 6020 Innsbruck, Austria